JGR Atmospheres

RESEARCH ARTICLE
10.1029/2024JD041726

Processes Driving the Intermodel Spread of the Southern Hemisphere Hadley Circulation Expansion in CMIP6 Models

Ije Hur[1], Changhyun Yoo[1], Sang-Wook Yeh[2], Young-Ha Kim[3], and Kyong-Hwan Seo[4,5]

[1]Department of Climate and Energy Systems Engineering, Ewha Womans University, Seoul, South Korea, [2]Department of Marine Science and Convergence Engineering, Hanyang University, ERICA, Ansan, South Korea, [3]Research Institute of Basic Sciences, Seoul National University, Seoul, South Korea, [4]Department of Atmospheric Sciences, Pusan National University, Busan, South Korea, [5]Institute for Future Earth, Pusan National University, Busan, South Korea

Abstract The Hadley circulation (HC) has been expanding poleward in recent decades. The Coupled Model Intercomparison Project Phase 6 (CMIP6) models predict that the expansion will accelerate in the future, more so in the Southern Hemisphere (SH). However, the extent of the expansion varies widely among the models. We investigate the mechanisms driving the intermodel spread in SH HC expansion predictions. The intermodel spread is obtained by an empirical orthogonal function analysis on the SH HC trend patterns of 16 CMIP6 model simulations using the historical and shared socioeconomic pathway 5–8.5 scenarios. The leading mode, showing a mean meridional stream function anomaly at the poleward SH HC extent, explains 49.73% of the variance and significantly correlates ($r = 0.94$) with the SH HC expansion. By analyzing the extended Kuo-Eliassen equation, we find that the intermodel difference in the representation of diabatic heating is responsible for about 14% of the intermodel spread. The meridional eddy momentum and heat fluxes contribute to about 21% and 18% of the intermodel spread, respectively. The models simulating a relatively large SH HC expansion tend to show increased precipitation in the Southern Pacific Convergence Zone, reduced baroclinic instability in the subtropics, and an enhanced poleward shift of jet stream in the midlatitudes. This suggests that the uncertainty in the HC projection may be constrained by reducing the bias in the trend of the mean fields.

Plain Language Summary The Hadley circulation (HC), which affects global climate patterns, is expanding toward the poles. However, different climate models predict varying extents of this expansion, especially in the Southern Hemisphere (SH). We aim to understand why. By analyzing climate model data, we identified key factors influencing the spread in SH HC expansion. Our findings suggest that factors like diabatic heating and meridional eddy momentum play significant roles. Models showing greater SH HC expansion tend to simulate increased precipitation in specific regions and shifts in atmospheric jet streams. Addressing these model biases could help reduce uncertainty in future HC projections.

Key Points:

- The first intermodel stream function trend mode effectively captures the spread of the Southern Hemisphere Hadley Circulation expansion
- The intermodel spread in expansion is explained by the spread of the meridional eddy momentum, heat fluxes, and diabatic heating
- The spread of the eddy fluxes and diabatic heating are linked with the changes in precipitation, jet, and static stability

Supporting Information:

Supporting Information may be found in the online version of this article.

Correspondence to:

C. Yoo,
cyoo@ewha.ac.kr

Citation:

Hur, I., Yoo, C., Yeh, S.-W., Kim, Y.-H., & Seo, K.-H. (2024). Processes driving the intermodel spread of the Southern Hemisphere Hadley Circulation expansion in CMIP6 models. *Journal of Geophysical Research: Atmospheres*, *129*, e2024JD041726. https://doi.org/10.1029/2024JD041726

Received 2 JUN 2024
Accepted 16 OCT 2024

1. Introduction

The Hadley circulation (HC), a meridional overturning circulation in the tropics, has been observed to expand poleward in recent decades (e.g., Hu et al., 2013; Johanson & Fu, 2009; Seidel et al., 2008; Staten et al., 2019). Since 1979, the magnitude of the tropical expansion has been about 0.1°–0.5° per decade, although the exact value varies between the hemispheres and depends on the measurement metrics and data sets used (e.g., Nicholas Davis & Birner, 2017; NA Davis & Davis, 2018; Staten et al., 2019). Both anthropogenic forcing and natural variability are reported to be responsible for the observed expansion (e.g., Allen & Kovilakam, 2017; Amaya et al., 2018; Garfinkel et al., 2015; Gerber & Son, 2014; Grise et al., 2019; Lau & Kim, 2015; Min & Son, 2013). Climate models show that increases in greenhouse gas concentrations, stratospheric ozone depletion, and anthropogenic aerosols can lead to a broadening of the HC, while natural variability, such as the Pacific Decadal Oscillation, has also contributed (Grise et al., 2019).

The projected expansion of the HC is more pronounced under future climates (Grise & Davis, 2020; Hu et al., 2013; Hur et al., 2022; Lau & Kim, 2015; Xia et al., 2020). By 2100, the Southern Hemisphere (SH) and Northern Hemisphere expansions are expected to reach about 2° and 1°, respectively, relative to 1920–1960, as measured by the multimodel ensemble means of the Coupled Model Intercomparison Project Phase 5 (CMIP5) and Phase 6 (CMIP6) simulations under the Representative Concentration Pathway 8.5 or Shared Socioeconomic

Pathway (SSP) 5–8.5 scenarios (Grise & Davis, 2020). However, individual model projections of SH HC expansion show a wide range of about 3°. For example, in the KACE-1-0-G model, the SH HC is projected to increase to about 33.4°S in 2100, about 1.1° further south than the multimodel mean (MMM) of 32.3°S (Hur et al., 2022). This intermodel spread in the magnitude of HC expansion is generally attributed to differences in model sensitivity to external forcing and internal variability. However, the physical processes responsible for the intermodel spread in HC expansion are not well understood.

Previous studies have analyzed the intermodel spread of HC climatology over the historical period. An intermodel empirical orthogonal function (EOF) analysis of the climatological HC patterns of climate models identified a mode that explains most of the intermodel variance in the HC extent (Wang et al., 2020). The mode, which exhibits a mean meridional stream function anomaly at the poleward extent of the HC, was associated with a La Niña-like sea surface temperature (SST) anomaly in the tropical Pacific. The SST anomaly can influence the HC through its modulation of convective heating in the tropics or through its effects on the subtropical and extra-tropical circulations, and hence, the eddies (Feng et al., 2024; Zhang et al., 2023). However, the processes through which the modulation of the HC's extent occurs were not examined in these studies, and there remains a lack of understanding of how the spread between the models evolves.

The mean meridional circulation is governed by the physical processes associated with diabatic heating, meridional eddy momentum/heat fluxes, and zonal drag. A diagnostic equation, the Kuo-Eliassen (KE) equation (Peixoto & Oort, 1992), can be used to decompose and quantify the role of each forcing on the mean mass stream function (Kim & Lee, 2001). In a recent study, for example, the budget of the equation suggested that an incorrect representation of diabatic heating in reanalysis data sets may be responsible for the opposing trends in Northern Hemisphere HC strengthening between the CMIP5 and reanalyses (Chemke & Polvani, 2019). Also, a discrepancy between reanalyses in the multidecadal variability of HC strength is caused by a misrepresentation of diabatic heating associated with long-term climate modes, such as the Atlantic multidecadal oscillation (Zaplotnik et al., 2022). With respect to the extent of HC expansion, the eddy fluxes and diabatic heating biases explain the HC extent bias of a climate model, but the exact budget of the KE equation elucidating this bias has not been calculated (Hur et al., 2022). In the present study, we quantify the contributions of each term in the KE equation and examine the processes by which those terms induce the intermodel spread of the SH HC expansion predictions.

The aim of this study is to elucidate the intermodel spread across the CMIP6 climate models in representing the expansion of the annual mean SH HC. The investigation focuses on understanding the dynamic processes involved in the interactions between forcings from diagnostic equation and the SH HC. By applying an intermodel EOF analysis to the CMIP6 mass stream function trends, we identify an intermodel EOF pattern that explains the spread in the SH HC expansion. We then solve the extended KE equation to quantify the role of each term in the intermodel spread. Finally, we investigate the sources of the discrepancies by examining the diabatic heating, eddy fluxes, and background fields associated with the intermodel EOF.

The remainder of this paper is organized into three sections: Section 2 describes the reanalysis and model simulation data and the analysis methods. In Section 3, we present the results of the EOF analysis of the inter-model spread of the SH HC expansion predictions. In addition, we quantify how much of the HC expansion can be explained by the extended KE equation. Finally, the changes in the diabatic heating, eddy, and mean fields associated with the intermodel EOF are examined to verify which dynamical processes drive the intermodel spread. The conclusions we drew from this research and a discussion of these findings are presented in Section 4.

2. Data and Methods

2.1. Data

To examine the expansion of the HC in the past and future climate, we analyze CMIP6 model simulations forced by the historical (1850–2014) and the SSP5-8.5 (2015–2100) forcings. We select 16 models based on the availability of daily data and continuity of temporal coverage (Table S1 in Supporting Information S1). Since the study is concerned with long-term trends, monthly data with 19 vertical levels from 1,000 hPa to 1 hPa is used in most analyses except the KE equation calculations. The terms in the KE equation are calculated on a daily time scale, and the daily data have eight vertical levels from 1,000 hPa to 10 hPa. Both the monthly and daily data are originally available at different horizontal resolutions for different models (Table S1 in Supporting

Information S1). However, to compare intermodel trends, they are bilinearly interpolated to a resolution of 0.7° longitude × 0.7° latitude. The KACE-1-0-G model is excluded from the KE analysis because of unrealistic daily vertical winds, which has abnormally large values at the surface of continental boundaries and missing values in the upper troposphere.

The Japanese 55-year atmospheric reanalysis (JRA-55; Kobayashi et al., 2015) and the European Centre for Medium-Range Weather Forecasts reanalysis version 5 (ERA5; Hersbach et al., 2020) are used as references for the 1979–2020 period. Their horizontal resolutions are 1.25° longitude × 1.25° latitude and 1.5° longitude × 1.5° latitude, respectively.

2.2. Intermodel EOF Analysis of HC Trends

The HC is defined by a zonal mean mass stream function:

$$\overline{\Psi}_v(p,\ \phi) = \frac{2\pi a \cos(\phi)}{g} \int_p^0 \overline{v}(p,\ \phi)\, \mathrm{d}p\,. \tag{1}$$

Here, p is the pressure, ϕ is the latitude, a is the radius of the Earth, g is the gravitational acceleration, and the overbar denotes the zonal mean. Subscript v indicates that the stream function is defined using the meridional wind. Later, we will also define the stream function in terms of the KE equation.

The poleward extent of the SH HC is defined as the latitude, between 20°S and 50°S, where the annual mean $\overline{\Psi}$ at 500 hPa crosses from negative to positive. We note that the exact poleward extent is obtained by linearly interpolating $\overline{\Psi}$ at 500 hPa to find the zero-crossing latitude. The changes in the poleward extent (Δextent) are then measured as the linear trend of the annual mean value from 1850 to 2100.

The intermodel spread of SH HC expansion can be examined by applying the intermodel EOF to the HC trend patterns of the models. The HC trend pattern is obtained as the linear trend of $\overline{\Psi}$ over the 1850-2100 period for each model (i.e., $\Delta\overline{\Psi}$). We choose the analysis domain to be the latitudes from 15°S to 55°S, which covers the poleward branch of the SH HC. Similar EOF patterns are derived when the domain is extended to the entire globe or SH (not shown).

2.3. The Extended Kuo-Eliassen Equation

The mass stream function can be decomposed into contributions of the terms in the KE equation (Pikovnik, 2022). Such a decomposition has been employed to understand the mechanism and variability of the HC (Kim & Lee, 2001; Zaplotnik et al., 2022), as well as its intensity (Chemke & Polvani, 2019; Lachmy, 2022). We use the extended KE equation, which does not assume quasi-geostrophy. The KE-based stream function (i.e., $\overline{\Psi}_{\mathrm{KE}}$) has shown excellent agreement with $\overline{\Psi}_v$ in reanalyses (Zaplotnik et al., 2022). As shown in this paper, a reasonable agreement is found in the CMIP6 simulations. The extended KE equation is

$$\mathrm{L}\,\overline{\Psi}_{\mathrm{KE}} = \frac{R_d}{p}\frac{\partial \overline{Q}}{a\partial\phi} + f\frac{\partial^2 \overline{u'v'}\cos^2\phi}{a\cos^2\phi\partial p\partial\phi} - \frac{R_d}{p}\frac{\partial}{a\partial\phi}\left(\frac{\partial \overline{v'T'}\cos\phi}{a\cos\phi\partial\phi}\right) - f\frac{\partial \overline{X}}{\partial p} + f^2\frac{\partial \overline{u'\omega'}}{\partial p^2} + \frac{R_d}{p}\left(\frac{p}{p_0}\right)^{\frac{R_d}{c_p}}\frac{\partial}{a\partial\phi}\frac{\partial \overline{\omega'\theta'}}{\partial p}\,. \tag{2}$$

On the left-hand side, the second-order differential elliptic operator L (Peixoto & Oort, 1992) spatially enlarges the effect of the diagnostic terms on the right-hand side. The diagnostic terms represent the zonal mean diabatic heating ($\overline{Q}$), meridional eddy momentum flux ($\overline{u'v'}$), meridional eddy heat flux ($\overline{v'T'}$), zonal drag ($\overline{X}$), vertical eddy momentum flux ($\overline{u'\omega'}$), and vertical eddy heat flux ($\overline{\omega'\theta'}$). In these terms, u and ω are the zonal and vertical velocities, respectively; T is the temperature; θ is the potential temperature; and the prime symbol indicates that the variable is the deviation from the zonal mean. Other variables in Equation 2 include R_d, the idealized gas constant of dry air; p and p_0, the pressure and mean sea level pressure, respectively; a, the Earth's radius; f, the Coriolis parameter; and c_p, the specific heat capacity at constant pressure. The diabatic heating field and the zonal drag field are calculated as the residual of the thermodynamic equation and the zonal momentum equation under the assumption of a steady state, respectively (Zaplotnik et al., 2022).

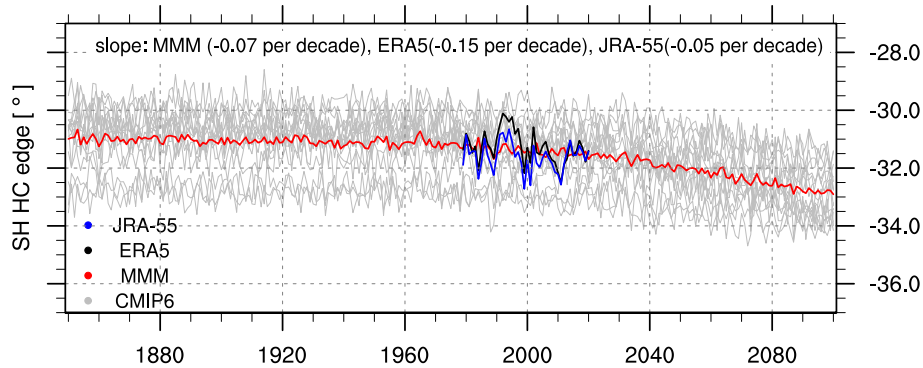

Figure 1. The annual mean time series of the SH HC extent at its poleward edge are shown for JRA55 and ERA5 during the 1979–2020 period as blue and black lines, respectively. The SH extents of historical and SSP5-8.5 CMIP6 model simulations are shown as gray lines for the 1850–2100 period. The multimodel mean of the CMIP6 models is shown as a red line. The trends of the data sets, obtained by the linear regression over the period from 1979 to 2020, are shown in the upper part of the panel in degrees per decade.

By applying the inverse Laplacian to each side, we can obtain the stream function in terms of the six diagnostic terms as

$$\overline{\Psi}_{\mathrm{KE}} = \overline{\Psi}_{\overline{Q}} + \overline{\Psi}_{\overline{u'v'}} + \overline{\Psi}_{\overline{v'T'}} + \overline{\Psi}_{\overline{X}} + \overline{\Psi}_{\overline{u'\omega'}} + \overline{\Psi}_{\overline{\omega'\theta'}}. \tag{3}$$

The HC trend associated with each term can be computed by taking the linear trend of each term in Equation 3. All the results of this calculation are then averaged to annual means to compare the trend pattern of the SH HC from each model.

3. Results

3.1. Intermodel EOF

The poleward expansion of the SH HC is evident in both reanalysis data sets and CMIP6 model simulations (Figure 1). In the JRA-55 and ERA5, the HC expands at a rate of about 0.05° and 0.15° per decade, respectively, over the 1979-2020 period. The difference between the reanalyses can be attributed to the lack of mass conservation in the data sets (NA Davis & Davis, 2018), but they showed poleward expansions with similar magnitude. During the same period, the MMM shows an average expansion rate of 0.07° per decade. The rate of expansion is predicted to accelerate toward the end of the 21st century (Grise & Davis, 2020). For the period 2021–2100, the MMM expansion rate is as much as ∼0.18° per decade.

The rate of expansion varies widely among the CMIP6 model simulations (gray lines in Figure 1). The MMM predicts an expansion of approximately 1.74° between 1850 and 2100. However, there is considerable variability among the individual model projections, with a range of approximately 2° across the models. Specifically, some models project slower rates of expansion, around 0.05° per decade (e.g., CMCC-CM2-SR5 and CMCC-ESM2), while others project faster rates, ranging from 0.11° to 0.13° per decade (e.g., UKESM1-0-LL to KACE-1-0-G). This indicates that the uncertainty in the HC expansion rate is as large as its mean projection, highlighting the importance of understanding the nature of the intermodel spread. Moreover, the models that have shown an excessive expansion in the recent period show even stronger acceleration in the future projection (Hur et al., 2022).

To understand the spread in the projected HC expansions, we apply an intermodel EOF analysis to the trend patterns of the mass stream function over the region from 15°S to 55°S (Figure 2). The intermodel EOFs describe the dominant patterns that explain much of the variance in the trends of the models, and their corresponding principal components (PCs) can be used to find the processes associated with the intermodel EOFs. We found that the first three modes explain ∼92% of the total variance across the models, and therefore neglect the modes that explain the remaining variance.

The leading mode (EOF1), which accounts for the 49.73% of the variance, has a negative anomaly centered at 35°S, accompanied by positive anomalies near 10°S and 60°S (shading in Figure 2a). The subtropical anomaly

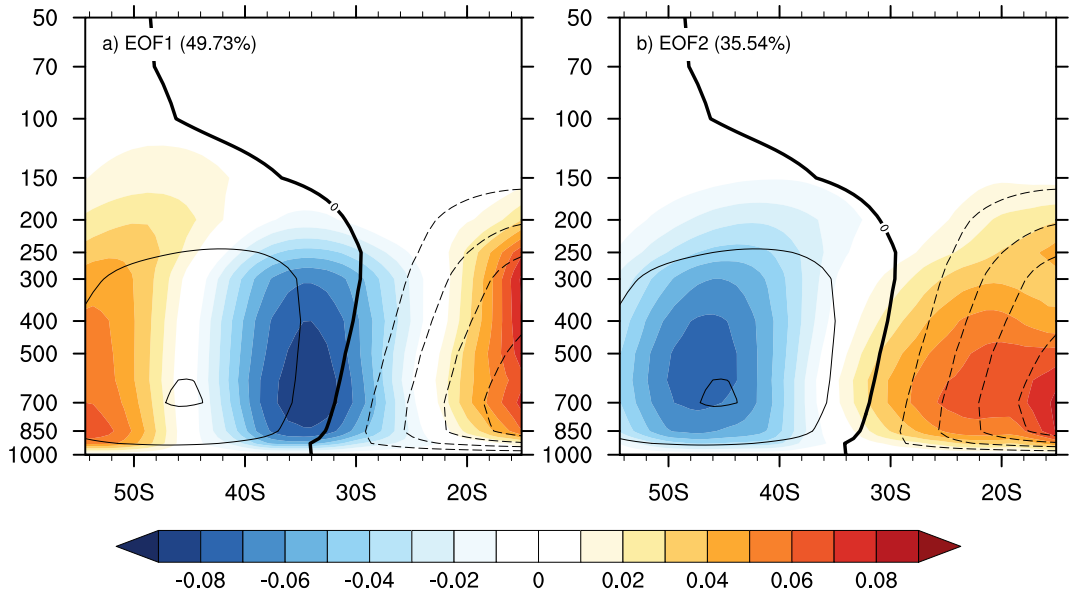

Figure 2. First and second modes of the normalized intermodel EOF patterns from the CMIP6 model trends (shading; 1850–2100) and the MMM stream function climatology (contour; 1850–1879). are shown Thin solid (dashed) contours are positive (negative) values, and the zero values are indicated by the thick solid contours. The contour interval is 2×10^{10} kg s^{-1}.

adjacent to the HC extent (thick solid contours in Figure 2) suggests a plausible correlation between PC1 of models and their HC expansion trend. The positive anomaly in the center of the SH HC in PC1 also implies a correlation with its strength trend. The anomalies in the second and third modes are located away from the poleward extent of the HC. The second mode explains 35.54% of the intermodel variance in the mean meridional stream function trend. Its pattern is concentrated in the center of the Ferrel cell, suggesting that it represents intermodel differences in changes of the circulation strength (not shown; Figure 2b). The third mode, explaining 6.66% of the variance, represents model differences in low latitude regions with a vertically tilted structure in the subtropics, which is related to the structural changes in the SH HC, not to the expansion (not shown).

To demonstrate that EOF1 alone can explain a large fraction of the variation in the HC expansion trend, we examine the relationship between the PCs and the HC expansion trend (Figure 3). It is evident that the models with positive and large PC1s tend to overestimate the HC expansion (Figure 3a). The Pearson correlation coefficient, r, between PC1 and the magnitude of Δextent for all models is approximately 0.94, and the significance of the correlation exceeded the 95% confidence level. Moreover, as in a previous study showing that weakening trends in SH HC strength predictions are accompanied by greater expansion under future climates (Chemke, 2021), PC1 also has a significant correlation of $r = 0.77$ with weakened SH HCs, though the correlation is not as strong as that between PC1 and expansion (not shown). In contrast, the correlations between Δextent and PC2 and between Δextent and PC3 are minimal, with coefficients of 0.02 and 0.09, respectively. Albeit not as closely as PC1, PC2 and PC3 are also associated with the weakening trend of the SH HC, with correlation coefficients of 0.46 and 0.37, respectively.

3.2. Reconstructing the Intermodel Spread Using the KE Equation

To use the extended KE equation, we first examine its accuracy in representing the mass stream function climatology and trend. To do this, we compare the stream function obtained directly from the meridional wind (Equation 1; Figure 4a) with the stream function computed by solving the extended KE equation (Equation 3; Figure 4c). The stream function field is compared in terms of three different quantities: the climatology over 1850–1879 period (green contours), the MMM trend (black contours), and the intermodel spread of stream function associated with the EOF1 (shading). Note that nonlinear shading intervals are chosen here and throughout the study to clearly show the extent of the mass stream function anomalies.

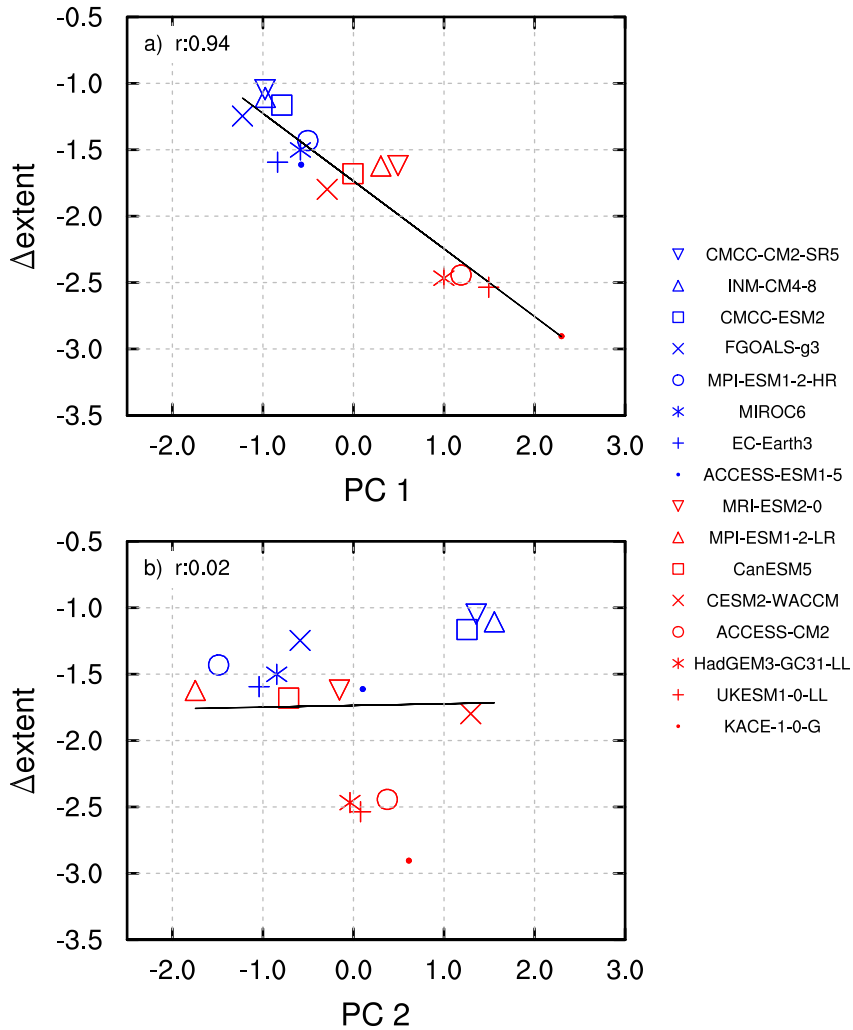

Figure 3. Scatter plots of the normalized principal components (PCs) and the predicted HC expansion between 1850 and 2100. The PCs correspond to the EOFs in Figure 2. The black line indicates the linear regression line of the two variables. The correlation coefficients are show in the upper left corner of each plot.

We find that the overall structures of the $\overline{\Psi}_v$ (Figure 4a) are reasonably reconstructed when all the terms of the extended KE equation (i.e., $\overline{\Psi}_{KE}$) are used (Figure 4c and Figure S1 in Supporting Information S1). First, for the climatology (green contours in Figure 4), the HCs defined by both methods are all centered near 15°S with their poleward extent near 30°S. The HC extent of the $\overline{\Psi}_{KE}$ is biased equatorward by 1° compared to that of the $\overline{\Psi}_v$, but the locations of the SH HC's poleward extent in the two methods show a significant correlation of $r = 0.98$ over 1850–2100 (Figure S2 in Supporting Information S1). Second, the MMM trend patterns of the two methods (black contours in Figure 4) show a negative stream function trend at the poleward extent of the SH HC, centered near 34°S. The two methods show a reasonable agreement in poleward expansion, with rates of about 0.07° and 0.06° per decade for $\overline{\Psi}_v$ and $\overline{\Psi}_{KE}$, respectively. The discrepancy in the trend patterns seen in the tropics does not have a substantial impact on the rate of HC expansion. Lastly, the intermodel spreads (shading in Figure 4) of the two methods show a tripolar pattern of stream function anomalies centered at about 15°S, 34°S, and 55°S. The amplitude at the poleward HC extent is somewhat overestimated when $\overline{\Psi}_{KE}$ is used (second column of Table 1). For example, a cross section at 500 hPa shows that the magnitude of the spread in the stream function trend based on $\overline{\Psi}_{KE}$ (purple line in Figure 6a) is 1.7 times greater than that based on $\overline{\Psi}_v$ (black line in Figure 6a; see also Table 1) by about 70%. However, the discrepancy becomes substantially reduced at lower pressure levels, such as 850 hPa (Figure 6b). At 850 hPa, the intermodel spread by $\overline{\Psi}_{KE}$ is about 22% stronger than that of $\overline{\Psi}_v$ over the domain between 29°S and 39°S (Table 1). This is still not a small difference, which may be inevitable due to the

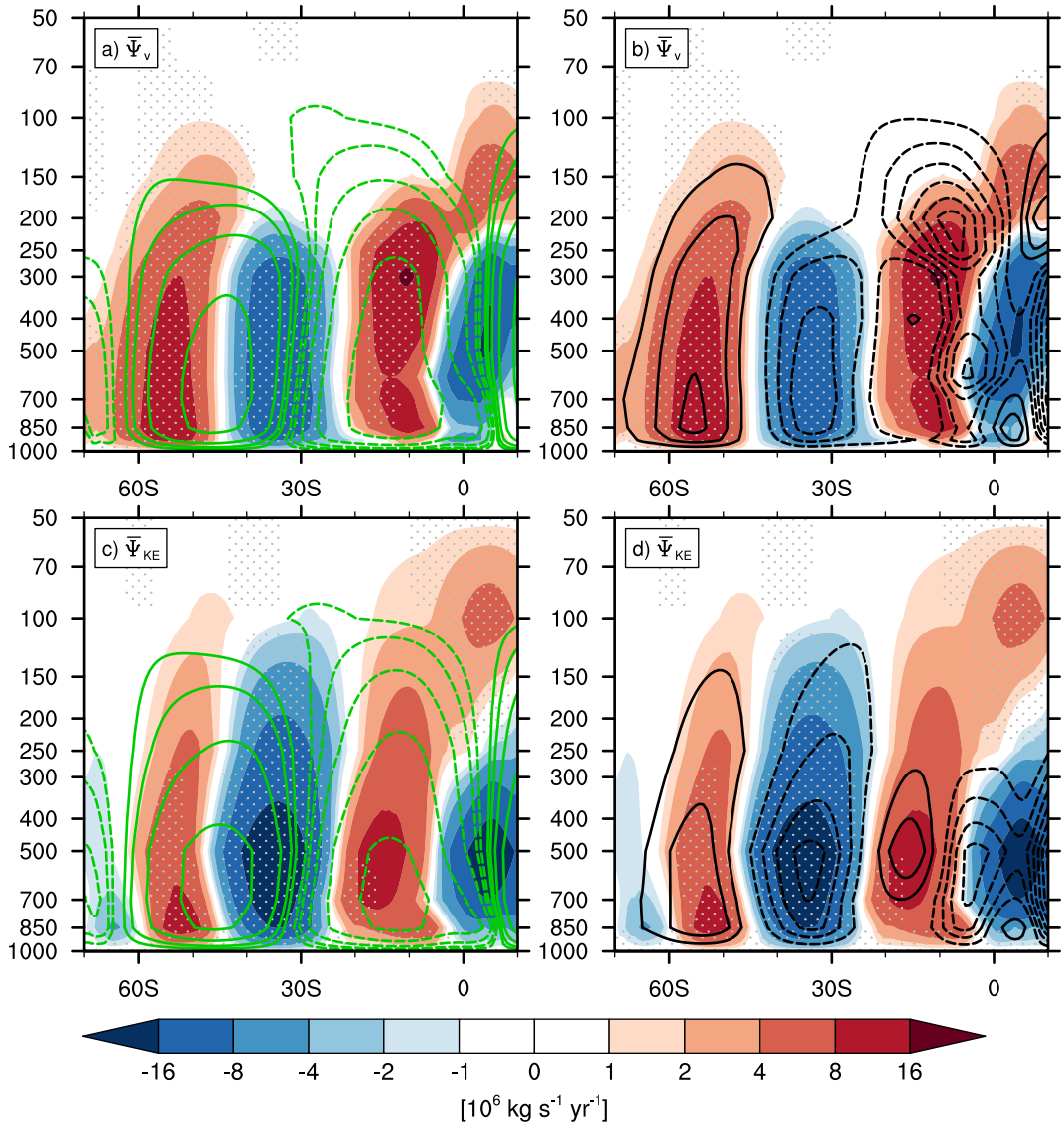

Figure 4. The mean meridional stream function based on the meridional wind ($\overline{\Psi}_v$; top) and the extended KE equation ($\overline{\Psi}_{KE}$; bottom). The green contours in the left panels indicate the MMM climatology (1850–1879), and the black contours in the right panels are the MMM trend. The shading is the intermodel spread pattern, which is regressed against PC1. The unit of the MMM climatology is 10^9 kg s^{-1}, and the unit of the MMM trend and intermodel spread are 10^6 kg s^{-1} yr^{-1}. The nonlinear shading interval used for intermodel spread is shown in the color bar. The same nonlinear intervals are selected for the contour intervals of both the climatology and the trend. Gray dots indicate the statistically significant at 95% confidence level.

Table 1
The Latitudinal Means (29°S–39°S) of the Intermodel Spread of the Stream Function Trend at Each Atmospheric Level in Figure 6 and Their Respective Ratios

Pressure level [hPa]	Ratio of $\overline{\Psi}_{KE}/\overline{\Psi}_v$	Ratio of each component over $\overline{\Psi}_{KE}$ [%]					
		$\overline{\Psi}_{\overline{Q}}$	$\overline{\Psi}_{\overline{u'v'}}$	$\overline{\Psi}_{\overline{v'T'}}$	$\overline{\Psi}_{\overline{X}}$	$\overline{\Psi}_{\overline{u'\omega'}}$	$\overline{\Psi}_{\overline{\omega'\theta'}}$
500	1.73	14.08	20.98	18.05	34.84	7.20	4.87
850	1.22	14.87	13.36	14.44	49.17	8.56	−0.41

Note. The Second Column Shows the Ratio of $\overline{\Psi}_{KE}/\overline{\Psi}_v$, Which Quantifies the Overall Accuracy of the Extended KE Equation Budget in Simulating the Intermodel Spread. The Ratios in the Third Through Sixth Columns Indicate the Contribution of Each Diagnostic Term, Represented as Percentiles Obtained by Dividing Each Diagnostic Term by $\overline{\Psi}_{KE}$.

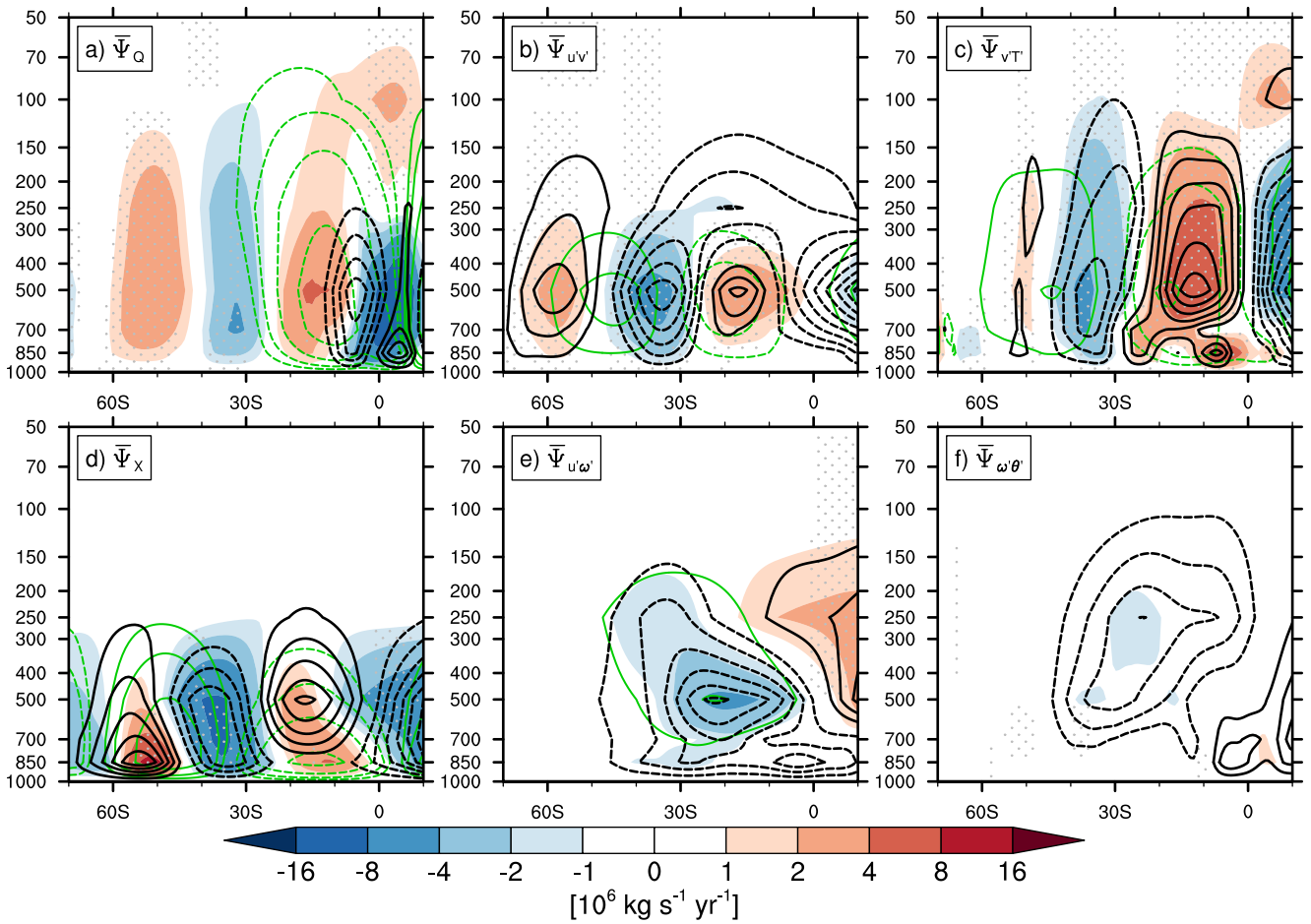

Figure 5. The stream function field associated with each forcing term in Equation 3. The stream function is reconstructed by the (a) the diabatic heating, (b) the meridional eddy momentum flux, (c) the meridional eddy heat flux, (d) the zonal drag, (e) the vertical eddy momentum flux, and (f) the vertical eddy heat flux. As in Figure 4, the shading represents the intermodel spread, which is regressed against PC1. The green contours show the MMM and climatology, and the black contours show the MMM trend of each term. Gray dots indicate the statistical significance at 95% confidence level.

limited number of vertical levels available for the daily CMIP6 data. Nevertheless, decomposition using the KE equation can be useful for characterizing the overall contributions of the forcing terms that result in the intermodel spread of the HC expansion predictions.

The intermodel spread of stream function trend inverted from each forcing term, shown in Figure 5, highlights the significant contributions of the quasi-geostrophic terms to the intermodel spread of the SH HC expansion (i.e., $\overline{\Psi}_{\overline{Q}}$, $\overline{\Psi}_{\overline{u'v'}}$, and $\overline{\Psi}_{\overline{v'T'}}$). First of all, the intermodel spread by the diabatic heating component ($\overline{\Psi}_{\overline{Q}}$; shading in Figure 5a) shows a characteristic tripole stream function pattern similar to the total stream function pattern seen as shading in Figure 4a. The characteristic pattern appears all for the cross sections at 500 and 850 hPa (i.e., blue line for $\overline{\Psi}_{\overline{Q}}$, black line for $\overline{\Psi}_v$, and purple line for $\overline{\Psi}_{\mathrm{KE}}$ in Figure 6). However, the ratio of the intermodel spread of $\overline{\Psi}_{\overline{Q}}$ to that of $\overline{\Psi}_{\mathrm{KE}}$, averaged over the 29°S–39°S region, is about 14.1% and 14.9% for 500 and 850 hPa, respectively (Table 1), implying a need to consider the roles of the other terms. The meridional eddy flux terms also make substantial contributions to the intermodel spread. The MMM trend and the intermodel spread by the meridional eddy momentum flux ($\overline{\Psi}_{\overline{u'v'}}$) both induce a negative stream function anomaly at 35°S (black contours and shading in Figure 5b). They are out of phase with the MMM climatology field (green contours in Figure 5b), being more poleward. This implies a poleward shift of $\overline{\Psi}_{\overline{u'v'}}$ in the future, and it indicates that the overexpanded models exhibit relatively stronger intensities in the trend of meridional eddy momentum-induced circulation in the subtropics. As a result, the eddy momentum flux term shows secondary importance, following the zonal drag, in explaining the intermodel spread, contributing 21.0% of the total amplitude at 500 hPa, with its impact decreasing

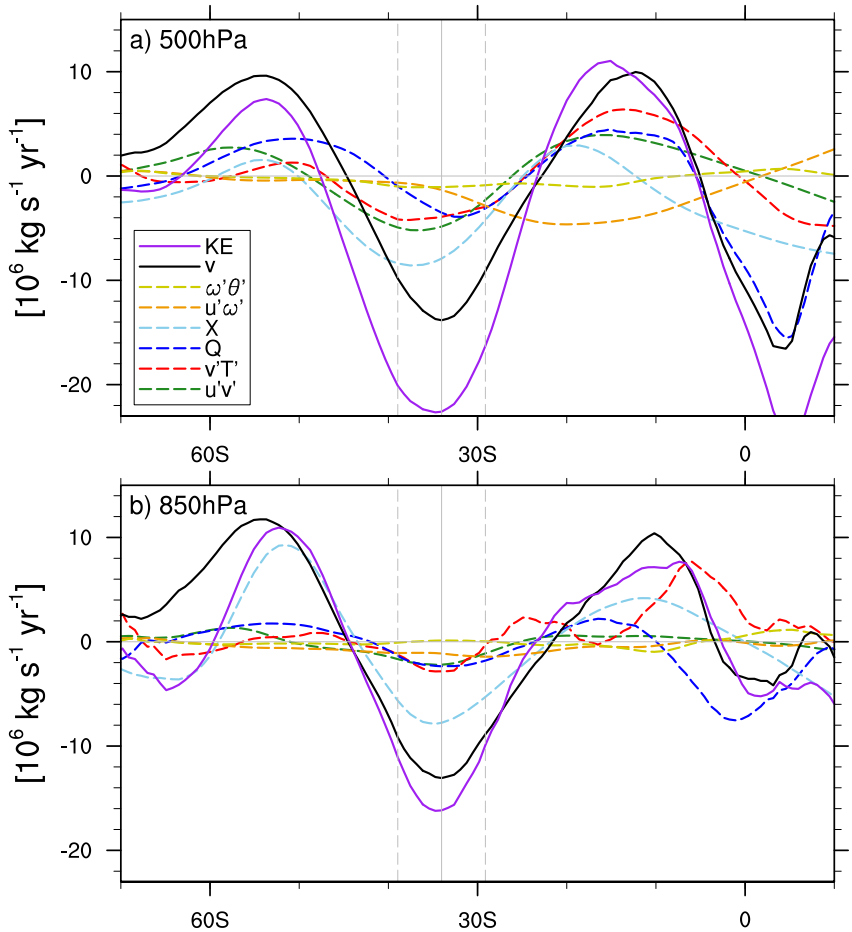

Figure 6. The vertical cross sections of the intermodel spread of the stream function trend in Figures 4 and 5 at 500 and 850 hPa. The stream function based on the meridional wind ($\overline{\Psi}_v$ in Figure 4) is represented by a black line and that of the extended KE equation ($\overline{\Psi}_{\mathrm{KE}}$ in Figure 4) by a purple line. The stream function based on the meridional eddy momentum ($\overline{\Psi}_{\overline{u'v'}}$ in Figure 5; green line), heat fluxes ($\overline{\Psi}_{\overline{v'T'}}$; red line), diabatic heating ($\overline{\Psi}_{\overline{Q}}$; blue line), zonal drag ($\overline{\Psi}_{\overline{X}}$; light-blue line), vertical eddy momentum ($\overline{\Psi}_{\overline{u'\omega'}}$; orange line), and heat fluxes and ($\overline{\Psi}_{\overline{\omega'\theta'}}$; yellow line) are shown. The gray solid line indicates 34°S, where the intermodel spread of $\overline{\Psi}_v$ (black line) has its minimum value, and the gray dashed lines indicate the 29°S–39°S range used to quantify the latitudinal mean in Table 1.

at the lower pressure level (green line in Figure 6 and Table 1). In comparison, the MMM trend and the intermodel spread of the meridional eddy heat flux-induced circulation ($\overline{\Psi}_{\overline{v'T'}}$) have a similar structure with that of $\overline{\Psi}_{\overline{u'v'}}$, but with more vertically stretched and concentrated subtropical cells (Figure 5c). The heat flux term explains 18.1% of the total amplitude of the intermodel spread at 500 hPa; however, its influence also decreases at the lower level (red line in Figure 6 and Table 1). The dynamical processes by which the forcing terms drive these circulation patterns are described in the next subsection.

The remaining three terms may be less important than the above three. This is despite the intermodel spread of a negative anomaly in the subtropics due to the zonal drag ($\overline{\Psi}_{\overline{X}}$) (Figure 5d). The negative anomaly of the zonal drag accounts for about 49.2% of the total stream function spread trend at 850 hPa, about the half of the total field, and its contribution at 500 hPa is still dominant with 34.8% (light blue line in Figure 6 and Table 1). However, it is crucial to consider that the circulation induced by zonal drag may be a passively modified consequence. Based on the zonal momentum equation, the balance between zonal drag and the Coriolis force at the surface induces westerlies (easterlies), inducing an indirect (direct) cell, through eddies in the midlatitudes (tropics) (Kim & Lee, 2001). These westerlies and easterlies could also be driven by the diabatic heat sources (Zaplotnik et al., 2022). Therefore, we conclude that the intermodel spread of the zonal drag can be interpreted as a result of

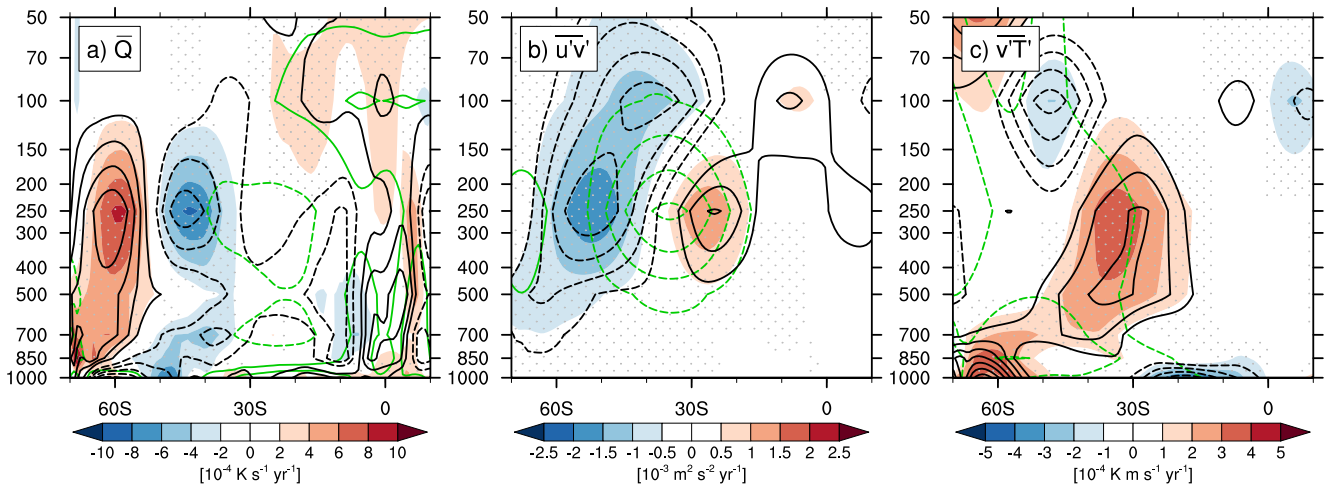

Figure 7. The intermodel spread of quasi-geostrophic diagnostic terms in Equation 2. The green contours indicate the MMM climatology (1850–1879), and the black contours are the MMM trend. The intermodel spread of the trend is indicated by the shading, with the shading interval shown in each panel. The contour interval of the trend (black) is set to twice the corresponding intermodel spread (shading). For example, the contour interval of the meridional eddy heat flux is 2×10^{-4} K m s^{-1} yr^{-1}. The contour intervals of the MMM climatologies are 0.5, except for the meridional eddy momentum flux, which is 1.5, all based on the International Standard of Units. Gray dots represent the statistical significance at 95% confidence level.

the above three quasi-geostrophic terms. Lastly, the vertical eddy momentum and heat fluxes also induce negative stream function spread trend anomalies (Figures 5e and 5f), but they are centered between 20°S and 30°S (orange and yellow lines in Figure 6), not poleward of 30°S. In addition, the vertical fluxes make negligible contributions to the intermodel spread of the negative anomaly (Figure 5f and yellow line in Figure 6).

3.3. The Forcing Terms and the Mean States Associated With the Intermodel Spread

In the last section, diabatic heating and meridional eddy fluxes were found to be the major contributors to the intermodel spread of the HC expansion. Next, we examine how the patterns of the forcing terms and the mean states are related to those of the intermodel spread.

The intermodel spread of the diabatic heating trend has a positive anomaly near 20°S and a negative anomaly near 40°S in the upper troposphere (shading in Figure 7a). Even the positive anomaly of the spread is located further poleward than the MMM trend. Recall from Equation 2 that the meridional gradient of the diabatic heating is negatively proportional to the stream function. Thus, the spread in the diabatic heating trend, forming an enhanced meridional gradient near 30°S, results in an intermodel spread of negative stream function trend. We find that the positive diabatic heating anomaly near 20°S is mainly due to the enhanced precipitation in the South Pacific Convergence Zone (SPCZ; Figures 8a and 8b). That is, the overexpanded models tend to simulate an increased precipitation trend in the SPCZ region. Additionally, the negative (positive) diabatic heating anomaly near 40°S (60°S) is presumably associated with a poleward shift of the storm track, in conjunction with a poleward shift of the eddy-driven jet, which is also reflected in the dry anomalies of precipitation trends and their corresponding model spread (Figures 8a and 8c).

The intermodel spread of the eddy meridional momentum flux trend shows a divergence near 35°S (shading in Figure 7b). This explains the negative spread of the circulation trend in the subtropics (shading in Figure 5b), as the meridional and vertical gradients of the momentum flux are negatively proportional to the stream function (Equation 2). Also, the subtropical divergence of the momentum is consistent with the poleward jet shift because it weakens the zonal wind near 35°S (shading in Figure 8c).

The intermodel spread of the eddy meridional heat flux trend shows a positive anomaly near 35°S (shading in Figure 7c), which induces a negative intermodel spread stream function trend in the same region (shading in Figure 5c; see also Equation 2). This positive heat flux anomaly is consistent with a reduced tropospheric meridional temperature gradient of intermodel spread trend pattern (shading in Figure 8d). Additionally, there is a negative heat flux trend and intermodel spread anomaly between 0° and 30°S near the surface (black contour and

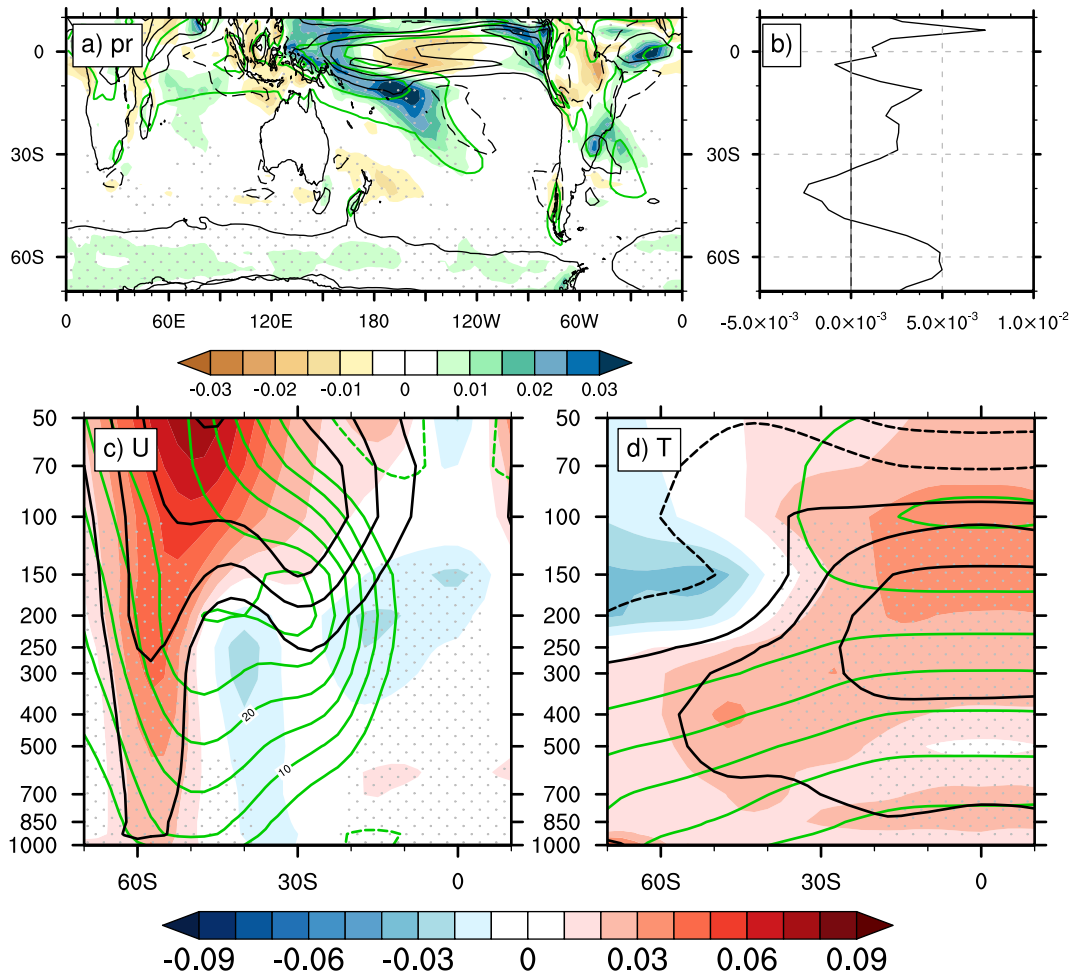

Figure 8. (a) The precipitation trend (mm day^{-1} decade^{-1}), (b) zonal mean of the precipitation trend (i.e., the zonal mean values of a; mm day^{-1} decade^{-1}), (c) zonal mean zonal wind trend (m s^{-1} decade^{-1}), and (d) zonal mean temperature trend (K decade^{-1}) regressed against PC1 are shown by shading. The MMM trends and climatologies are superimposed as black and green contours, respectively. The trend contours of the precipitation (a) are shown from −0.08 to 0.14 mm day^{-1} decade^{-1}, with an interval of 0.04 mm day^{-1} decade^{-1}, that of the zonal mean zonal wind (c) are shown from 0.1 to 0.4 m s^{-1} decade^{-1}, with an interval of 0.1 m s^{-1} decade^{-1}, and those of the zonal mean temperature (d) are shown from −0.2 to 0.3 K decade^{-1}, with an interval of 0.1 K decade^{-1}. The climatology contour intervals are 4 mm day^{-1}, 5 m s^{-1}, and 15 K. Solid (dashed) contours indicate positive (negative) values, and the zero contours are omitted. Gray dots indicate the statistically significant at 95% confidence level.

shading in Figure 7c, respectively). This results in a positive stream function trend, as seen in Figure 5c, partially offsetting but not reversing the negative trend induced by the heat flux at 35°S (not shown).

The zonal drag has a large spread, but it is primarily near the surface (Figure S3a in Supporting Information S1). This is consistent with the zonal drag spread being passively induced by the jet shift. The vertical momentum and heat fluxes show spreads that project onto their corresponding MMM trend patterns (Figures S3b–c in Supporting Information S1), which make small contributions to the stream function between 30°S and 40°S.

The intermodel spread in the basic states (shading in Figures 8c and 8d) roughly resembles the corresponding MMM trend pattern (black contours in Figures 8c and 8d), and the MMM trend patterns are understood as a response to anthropogenic forcing. For example, the MMM trend pattern in the zonal wind (black contours in Figure 8c) shows a poleward-shifted midlatitude jet relative to the climatological jet near 45°S (green contours in Figure 8c). This is a well-known response pattern to increasing greenhouse gas concentrations and decreasing stratospheric ozone (e.g., Lee & Feldstein, 2013; Shaw & Voigt, 2015; Son et al., 2010; Woollings et al., 2023). Strengthened vertical wind shear indicates enhanced baroclinicity near 35°S. The MMM trend in the zonal mean

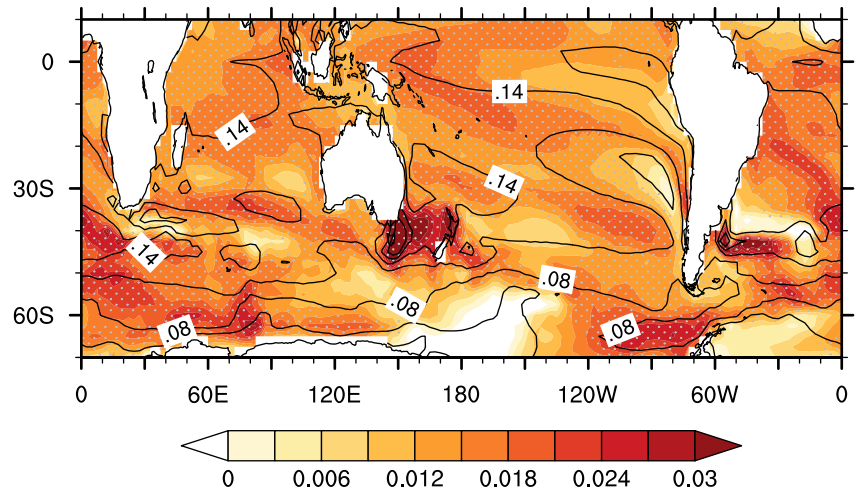

Figure 9. As in Figure 8, the patterns of SST (K decade^{-1}) regressed against PC1 are shown by shading. The MMM trends are superimposed as black contours with an interval of 0.03 K decade^{-1}. Gray dots indicate the statistical significance at 95% confidence level.

temperature field (black contours in Figure 8d), which is in thermal wind balance with the wind field, is also a forced response to the anthropogenic forcing. Consistent with the vertical wind shear, the meridional temperature gradient is enhanced around 35°S near the tropopause. The resemblance between the MMM trend (black contours) and the intermodel spread (shading) suggests that the models that are more sensitive to the forcing tend to predict greater HC expansion. Also found in the basic states is an increase in static stability in the subtropics (shading in Figure 8d). Increased static stability in the subtropics is a factor that can modulate the HC's strength and expansion by stabilizing the eddy growth and deflecting its propagation toward the poles (Lu et al., 2008; Seo et al., 2023; Yang et al., 2023).

4. Conclusions and Discussion

In this study, we investigated the physical processes driving the intermodel spread with respect to the SH HC expansion among CMIP6 models. We found that the spread is explained by the leading mode of the intermodel mass stream function trend fields. The processes associated with this mode were then examined using the extended KE equation. The main results can be summarized as follows.

- The first mode effectively captures the intermodel spread of SH HC expansion predictions. It explains 49.73% of the variance in the HC expansion trends across the CMIP6 models, and its PC time series shows a significant correlation, $r = 0.94$, with the models' HC expansions.
- The intermodel spread in HC expansion is primarily the result of the contributions of quasi-geostrophic terms, that is, the diabatic heating, the meridional eddy momentum, and heat fluxes. The extended KE equation shows that about 14.1%, 21.0%, and 18.1% of the negative subtropical stream function anomaly at 500 hPa are due to these three terms, respectively.
- The diabatic heating between 20°S and 40°S, which is responsible for the intermodel spread in the HC expansion predictions, is related to how the models simulate the precipitation trend in the SPCZ region (i.e., the meridional shift of the midlatitude jet). The intermodel spread in the meridional momentum and heat fluxes is linked with changes in static stability in the subtropics and the meridional shift of the eddy-driven jet.
- Zonal drag is found to be a large contributor to the intermodel spread of the HC expansion. However, we interpret that the role of the zonal drag is limited because the term is indirectly determined by the zonal wind.

For diabatic heating, it is important how models project changes in boundary conditions such as SST. We find that a large poleward expansion of the SH HC is associated with enhanced warming from the equatorial western Pacific into the SPCZ region (shading in Figure 9), in contrast to the MMM trend pattern of an El Niño-like warming SST trend (black contours in Figure 9). The SST warming in the subtropics may be related to model spread in cloud radiative processes over the Southern Ocean resulting from biases in shortwave cloud radiative

effects (Grise & Polvani, 2014; Kelleher & Grise, 2019). In addition, warming over the SPCZ region has been associated with increased precipitation (Folland et al., 2002), leading to the spread in diabatic heating.

In the budget calculation of the KE equation, some mismatch between the $\overline{\Psi}_v$ and $\overline{\Psi}_{\mathrm{KE}}$ existed. This is in part due to the sparse vertical resolution of the model data. With only nine vertical levels available for the daily data, we may not have been able to accurately represent the structures in the eddy flux and diabatic forcing fields. This may be especially true when the diabatic heating and zonal drag fields are computed as the residuals of the thermodynamic and zonal momentum equations, respectively. Nonetheless, the budget effectively shed light on the physical processes that govern the HC expansion in climate models.

This study can be improved in two key areas. First, previous studies have shown that changes in static stability and meridional temperature gradient can significantly influence trends in HC intensity (Chemke & Polvani, 2019) and extent (Seo et al., 2023; Yang et al., 2020). To further understand their role in the intermodel spread, changes in the Laplacian in the extended KE equation can be quantified (Kim & Lee, 2001; Zaplotnik et al., 2022). In addition, the forcing terms, such as eddy fluxes and diabatic heating, can be influenced by the background field, which can be influenced by other factors, such as oceanic processes. Modeling studies can help elucidate the causality between the forcing terms and the changes in the background field (Yang et al., 2023).

Data Availability Statement

The Japanese 55-year Reanalysis (JRA55; Kobayashi et al., 2015) can be downloaded from DIAS, https://diasjp.net/en/. The ECMWF Reanalysis v5 (ERA5; Hersbach et al., 2020) is accessible via https://www.ecmwf.int/en/forecasts/dataset/ecmwf-reanalysis-v5. CMIP6 data can be found at https://esgf-node.llnl.gov/search/cmip6/ (CMIP6 models are listed in Table S1 in Supporting Information S1). The Python code to solve the extended KE equation is available on Zenodo repository (Pikovnik, 2022).

Acknowledgments
This research was supported by the Korea Environmental Industry and Technology Institute through grant KEITI-2022003560001. I.H. and C.Y. are also supported by the specialized university program for confluence analysis of Weather and Climate Data of the Korea Meteorological Institute and by the National Research Foundation of Korea through grant RS-2024-00333469. K.H.S. is supported by Learning and Academic research institution for Master's·PhD students, and Postdocs (LAMP) Program of the National Research Foundation of Korea grant funded by the Ministry of Education (RS-2023-00301938).

References

Allen, R. J., & Kovilakam, M. (2017). The role of natural climate variability in recent tropical expansion. *Journal of Climate*, *30*(16), 6329–6350. https://doi.org/10.1175/JCLI-D-16-0735.1

Amaya, D. J., Siler, N., Xie, S.-P., & Miller, A. J. (2018). The interplay of internal and forced modes of hadley cell expansion: Lessons from the global warming hiatus. *Climate Dynamics*, *51*(1), 305–319. https://doi.org/10.1007/s00382-017-3921-5

Chemke, R. (2021). Future changes in the hadley circulation: The role of ocean heat transport. *Geophysical Research Letters*, *48*(4), e2020GL091372. https://doi.org/10.1029/2020GL091372

Chemke, R., & Polvani, L. M. (2019). Opposite tropical circulation trends in climate models and in reanalyses. *Nature Geoscience*, *12*(7), 528–532. https://doi.org/10.1038/s41561-019-0383-x

Davis, N., & Birner, T. (2017). On the discrepancies in tropical belt expansion between reanalyses and climate models and among tropical belt width metrics. *Journal of Climate*, *30*(4), 1211–1231. https://doi.org/10.1175/JCLI-D-16-0371.1

Davis, N., & Davis, S. M. (2018). Reconciling Hadley cell expansion trend estimates in reanalyses. *Geophysical Research Letters*, *45*(20), 11439–411466. https://doi.org/10.1029/2018GL079593

Feng, J., Wang, S., & Li, J. (2024). Strengthened ENSO amplitude contributed to regime shift in the hadley circulation. *Geophysical Research Letters*, *51*(2), e2023GL106006. https://doi.org/10.1029/2023GL106006

Folland, C., Renwick, J., Salinger, M., & Mullan, A. (2002). Relative influences of the interdecadal Pacific oscillation and ENSO on the South Pacific convergence zone. *Geophysical Research Letters*, *29*(13), 21–24. https://doi.org/10.1029/2001GL014201

Garfinkel, C. I., Waugh, D. W., & Polvani, L. M. (2015). Recent Hadley cell expansion: The role of internal atmospheric variability in reconciling modeled and observed trends. *Geophysical Research Letters*, *42*(24), 10824–810831. https://doi.org/10.1002/2015GL066942

Gerber, E. P., & Son, S.-W. (2014). Quantifying the summertime response of the austral jet stream and hadley cell to stratospheric ozone and greenhouse gases. *Journal of Climate*, *27*(14), 5538–5559. https://doi.org/10.1175/JCLI-D-13-00539.1

Grise, K. M., & Davis, S. M. (2020). Hadley cell expansion in CMIP6 models. *Atmospheric Chemistry and Physics*, *20*(9), 5249–5268. https://doi.org/10.5194/acp-20-5249-2020

Grise, K. M., Davis, S. M., Simpson, I. R., Waugh, D. W., Fu, Q., Allen, R. J., et al. (2019). Recent tropical expansion: Natural variability or forced response? *Journal of Climate*, *32*(5), 1551–1571. https://doi.org/10.1175/JCLI-D-18-0444.1

Grise, K. M., & Polvani, L. M. (2014). Southern hemisphere cloud–dynamics biases in CMIP5 models and their implications for climate projections. *Journal of Climate*, *27*(15), 6074–6092. https://doi.org/10.1175/JCLI-D-14-00113.1

Hersbach, H., Bell, B., Berrisford, P., Hirahara, S., Horányi, A., Muñoz-Sabater, J., et al. (2020). The ERA5 global reanalysis. *The Quarterly Journal of the Royal Meteorological Society*, *146*(730), 1999–2049. [Dataset]. https://doi.org/10.1002/qj.3803

Hu, Y., Tao, L., & Liu, J. (2013). Poleward expansion of the hadley circulation in CMIP5 simulations. *Advances in Atmospheric Sciences*, *30*(3), 790–795. https://doi.org/10.1007/s00376-012-2187-4

Hur, I., Kim, M., Kwak, K., Sung, H. M., Byun, Y.-H., Song, H., & Yoo, C. (2022). Hadley circulation in the present and future climate simulations of the K-ace model. *Asia-Pac. J. Atmospheric Sci.*, *58*(3), 353–363. https://doi.org/10.1007/s13143-021-00256-z

Johanson, C. M., & Fu, Q. (2009). Hadley cell widening: Model simulations versus observations. *Journal of Climate*, *22*(10), 2713–2725. https://doi.org/10.1175/2008JCLI2620.1

Kelleher, M. K., & Grise, K. M. (2019). Examining Southern Ocean cloud controlling factors on daily time scales and their connections to midlatitude weather systems. *Journal of Climate*, *32*(16), 5145–5160. https://doi.org/10.1175/JCLI-D-18-0840.1

Kim, H.-k., & Lee, S. (2001). Hadley cell dynamics in a primitive equation model. Part II: Nonaxisymmetric flow. *Journal of the Atmospheric Sciences*, *58*(19), 2859–2871. https://doi.org/10.1175/1520-0469(2001)058<2859:HCDIAP>2.0.CO;2

Kobayashi, S., Ota, Y., Harada, Y., Ebita, A., Moriya, M., Onoda, H., et al. (2015). The JRA-55 reanalysis: General specifications and basic characteristics. *Journal Meteorological Society Jpn. Ser. II*, *93*(1), 5–48. [Dataset]. https://doi.org/10.2151/jmsj.2015-001

Lachmy, O. (2022). The relation between the latitudinal shifts of midlatitude diabatic heating, eddy heat flux, and the eddy-driven jet in CMIP6 models. *Journal of Geophysical Research: Atmospheres*, *127*(16), e2022JD036556. https://doi.org/10.1029/2022JD036556

Lau, W. K. M., & Kim, K.-M. (2015). Robust Hadley Circulation changes and increasing global dryness due to CO^2 warming from CMIP5 model projections. *Proceedings of the National Academy of Sciences of the United States of America*, *112*(12), 3630–3635. https://doi.org/10.1073/pnas.1418682112

Lee, S., & Feldstein, S. B. (2013). Detecting ozone- and greenhouse gas–driven wind trends with observational data. *Science*, *339*(6119), 563–567. https://doi.org/10.1126/science.1225154

Lu, J., Chen, G., & Frierson, D. M. (2008). Response of the zonal mean atmospheric circulation to El Niño versus global warming. *Journal of Climate*, *21*(22), 5835–5851. https://doi.org/10.1175/2008JCLI2200.1

Min, S.-K., & Son, S.-W. (2013). Multimodel attribution of the Southern Hemisphere Hadley cell widening: Major role of ozone depletion. *Journal of Geophysical Research: Atmospheres*, *118*(7), 3007–3015. https://doi.org/10.1002/jgrd.50232

Peixoto, J. P., & Oort, A. H. (1992). *Physics of climate*. American Institute of Physics.

Pikovnik, M. (2022). mpikovnik/Evaluating-contributions-to-global-Hadley-cell-using-Kuo-Eliassen-equation: March 12, 2022 Release (Version 1.0) [Software]. *Zenodo*. https://doi.org/10.5281/zenodo.6349274

Seidel, D. J., Fu, Q., Randel, W. J., & Reichler, T. J. (2008). Widening of the tropical belt in a changing climate. *Nature Geoscience*, *1*, 21–24. https://doi.org/10.1038/ngeo.2007.38

Seo, K.-H., Yoon, S.-P., Lu, J., Hu, Y., Staten, P. W., & Frierson, D. M. W. (2023). What controls the interannual variation of hadley cell extent in the northern hemisphere: Physical mechanism and empirical model for edge variation. *npj Climate Atmosphere Science*, *6*(1), 204. https://doi.org/10.1038/s41612-023-00533-w

Shaw, T. A., & Voigt, A. (2015). Tug of war on summertime circulation between radiative forcing and sea surface warming. *Nature Geoscience*, *8*(7), 560–566. https://doi.org/10.1038/ngeo2449

Son, S.-W., Gerber, E. P., Perlwitz, J., Polvani, L. M., Gillett, N. P., Seo, K.-H., et al. (2010). Impact of stratospheric ozone on southern hemisphere circulation change: A multimodel assessment. *Journal of Geophysical Research*, *115*(D3). https://doi.org/10.1029/2010JD014271

Staten, P. W., Grise, K. M., Davis, S. M., Karnauskas, K., & Davis, N. (2019). Regional widening of tropical overturning: Forced change, natural variability, and recent trends. *Journal of Geophysical Research: Atmospheres*, *124*(12), 6104–6119. https://doi.org/10.1029/2018JD030100

Wang, C., Hu, Y., Wen, X., Zhou, C., & Liu, J. (2020). Inter-model spread of the climatological annual mean Hadley circulation and its relationship with the double ITCZ bias in CMIP5. *Climate Dynamics*, *55*(9), 2823–2834. https://doi.org/10.1007/s00382-020-05414-z

Woollings, T., Drouard, M., O'Reilly, C. H., Sexton, D. M. H., & McSweeney, C. (2023). Trends in the atmospheric jet streams are emerging in observations and could be linked to tropical warming. *Communication Earth Environment*, *4*(1), 125. https://doi.org/10.1038/s43247-023-00792-8

Xia, Y., Hu, Y., & Liu, J. (2020). Comparison of trends in the Hadley circulation between CMIP6 and CMIP5. *Science Bulletin*, *65*(19), 1667–1674. https://doi.org/10.1016/j.scib.2020.06.011

Yang, H., Lohmann, G., Lu, J., Gowan, E. J., Shi, X., Liu, J., & Wang, Q. (2020). Tropical expansion driven by poleward advancing midlatitude meridional temperature gradients. *Journal of Geophysical Research: Atmospheres*, *125*(16), e2020JD033158. https://doi.org/10.1029/2020JD033158

Yang, H., Lohmann, G., Shi, X., & Müller, J. (2023). Evaluating the mechanism of tropical expansion using idealized numerical experiments. *Ocean-land-atmosphereic Research*, *2*, 0004. https://doi.org/10.34133/olar.0004

Zaplotnik, Ž., Pikovnik, M., & Boljka, L. (2022). Recent hadley circulation strengthening: A trend or multidecadal variability? *Journal of Climate*, *35*(13), 4157–4176. https://doi.org/10.1175/JCLI-D-21-0204.1

Zhang, S., Hu, Y., & Liu, J. (2023). Inter-model spreads of the climatological mean Hadley circulation in AMIP/CMIP6 simulations. *Climate Dynamics*, *61*(9–10), 4411–4427. https://doi.org/10.1007/s00382-023-06813-8